Evolution of Microscopic Localization in Graphene in a Magnetic Field from Scattering Resonances to Quantum Dots

Suyong Jung[1,2*], Gregory M. Rutter[1*], Nikolai N. Klimov[1-3], David B. Newell[3], Irene Calizo[4], Angela R. Hight-Walker[4], Nikolai B. Zhitenev[1†], and Joseph A. Stroscio[1†]

[1]Center for Nanoscale Science and Technology, NIST, Gaithersburg, MD 20899
[2]Maryland NanoCenter, University of Maryland, College Park, MD 20742
[3]Electronics and Electrical Engineering Laboratory, NIST, Gaithersburg, MD 20899
[4]Physics Laboratory, NIST, Gaithersburg, MD 20899

Graphene exhibits rich new physics and great promise for applications in electronics. The half-integer quantum Hall effect and high carrier mobility are critically dependent on interactions with impurities/substrates and localization of Dirac fermions in realistic devices. We microscopically study these interactions using scanning tunneling spectroscopy (STS) of exfoliated graphene on a SiO$_2$ substrate in an applied magnetic field. The magnetic field strongly affects the electronic behavior of the graphene; the states condense into well-defined Landau levels with a dramatic change in the character of localization. In zero magnetic field, weakly localized states are created by the substrate induced disorder potential. In strong magnetic fields, the two–dimensional electron gas breaks into a network of interacting quantum dots formed at the potential hills and valleys of the disorder potential. Our results demonstrate how graphene properties are perturbed by the disorder potential; a finding essential for the physics and applications of graphene.

The exposed and tunable two-dimensional graphene electronic system offers a convenient test bed for an understanding of microscopic transport processes and the physics of localization. Graphene's high transport carrier mobility and broad tunability of electronic properties promise

---

[*] These authors contributed equally to this work
[†] To whom correspondence should be addressed: nikolai.zhitenev@nist.gov, joseph.stroscio@nist.gov

multiple applications[1-3]. As in semiconductor devices, these features are ultimately determined by electron interactions and scattering from disorder including the surrounding environment of the device. Direct access to the graphene with scanned probes allows for the measurement of these interactions in greater detail[4-13] than possible in conventional semiconductor devices where the transport layers are buried below the surface. For example, STS with atomic resolution has been used[4,5] to study the local density of states of graphene and the role of disorder at zero magnetic field. Scanning single-electron transistor experiments, sensitive to local electric fields, produced local charge density maps with a spatial resolution of 150 nm[6] and detected single-electron charging phenomena at high magnetic fields[7].

In this article, we present STS measurements of a gated single-layer exfoliated graphene device in magnetic fields ranging from zero to the quantum Hall regime. With the ability to control the charge density of Dirac fermions with an electrostatic back gate with fine resolution, which was missing in previous STS studies[5,8-14], we can investigate local density of states and localization in graphene at the atomic scale while varying the Fermi energy (E_F) with respect to the Dirac (charge neutrality, E_D) point. At zero magnetic field, we observe density fluctuations arising from the disorder potential variations due to charged impurities underneath the graphene. At higher magnetic fields, discrete Landau levels (LLs) are resolved with both electron and hole states that follow single-layer graphene scaling. The LL spectra are dramatically different from previous STS measurements on epitaxial graphene on SiC[8,9,13] and graphene flakes on graphite[10,11], which are characteristic of weak disorder systems. Besides broader LLs due to disorder, we observe an additional set of localization resonances in the tunneling spectra, which are governed by single electron charging effects. Effectively, the localization in graphene can create a local quantum dot (QD)[7,15,16] with current flowing through two tunnel barriers in series;

2

one barrier being the vacuum tunnel barrier between the probe tip and a local graphene QD, and the other barrier originating from resistive incompressible strips that isolate the QD in high magnetic fields. As a result, our STS measurements can not only detect local density of state variations in graphene with/without magnetic fields, but we are also capable of measuring the graphene electronic structure with sensitivity to probe single-electron charging phenomena at the Fermi level.

Figure 1a shows a scanning tunneling microscopy (STM) topograph of single-layer graphene exfoliated on SiO_2/Si substrate (see supplemental material) over an area of 60 nm $\times$ 60 nm. The peak-to-peak height corrugation of 1.2 nm is presumably due to the surface roughness of the underlying SiO_2[4,17,18]. As shown in the inset of Fig. 1a, the graphene honeycomb lattice is clearly resolved in atomic resolution STM images in any of the local areas.

First, we turn our attention to how charged impurities and structural disorder affect the local electronic properties of graphene in zero magnetic field. In an ideal graphene layer, the carrier density can be continuously tuned from hole to electron doping through zero density at E_D. However, as illustrated in Fig. 1c, local disorder gives rise to a spatially varying electrostatic potential that changes the relative position of E_D with respect to E_F. By applying an external gate voltage, we can tune the level of the chemical potential, E_F with respect to E_D, switching the charge carriers between electrons and holes. If E_F is close to E_D, then spatially alternating patterns of electron and hole puddles are formed[4,6,19,20]. The variation of this local electrostatic potential has been considered as one of the main sources for the measured minimum conductivity in macroscopic graphene devices[20].

The distribution of the density set by the back gate voltage and spatially modulated by the disorder potential can be determined by locating E_D, a local minimum of the differential conductance dI/dV; a quantity that is proportional to the graphene local density of states. Figure 1d shows a representative dI/dV spectrum with two distinct minima observed at tunneling bias voltages $V_b = $ -140 mV and $V_b = 0$ mV. The minimum at $V_b = $ -140 mV corresponds to E_D while the zero-bias anomaly at $V_b = 0$ mV is characteristic of tunneling into graphene and other low-dimensional systems[5,14,21]. The zero-bias anomaly complicates an unambiguous E_D determination when the average density is set close to the neutrality point. By setting the average E_D away from zero bias and following the method developed in the reference 4, we obtain the spatial variation of E_D from the mapping of dI/dV at a fixed V_b close to the average E_D (Fig. 1b). The map provides an approximate landscape of the spatial distribution of the density fluctuations. Several distinct features with a characteristic length scale of 20 nm to 30 nm are identified by potential minima (pink colored region) and maxima (blue colored region). At low densities, these pink and blue areas would lead to electron and hole puddles, respectively.

While the approach described above provides a useful guide to identify the density fluctuations, accurate measurements of the fluctuations can be made only by finding the energy position of E_D from the individual spectra at each spatial point. Tracking E_D represented by a 'dip' in the dI/dV map in the vicinity of $V_b \approx $ -140 mV (Fig. 1e) yields a peak-to-peak variation of ≈ 20 meV in a given disorder potential, which corresponds to a density fluctuation of $\approx 3 \times 10^{11}$ cm^{-2}. Near the second minimum in the dI/dV spectrum in the vicinity of E_F (zero bias), we observe a series of sharp resonances with spacing of the order of ≈ 15 mV and linewidths of ≈ 10 mV (Figs. 1d and 1e). We attribute these resonances to scattering from impurities or the disorder

potential[5]. This interpretation is supported by the correlation between the spatial properties of the disorder potential and the spatial variation of the resonances (Figs. 1b and 1e).

More insight on the resonant peaks can be obtained from measuring *dI/dV* with respect to gate bias, i.e. gate mapping. The presence of the back gate controlling the charge density allows us to use a convenient approach to collecting and analyzing data in STS experiments as displayed in Figs. 2a and 2b. For a gate map, a series of *dI/dV* spectra is recorded as a function of both tunneling bias and gate voltages at a fixed spatial location. The Dirac point in zero magnetic field, represented by a *dI/dV* 'dip' in Fig. 2a varies in energy as a function of gate voltage. The dotted yellow line is from the best fit of the E_D evolution with the Fermi velocity of $(1.12 \pm 0.01) \times 10^6$ ms^{-1}, which agrees well with those from previously reported exfoliated[6,14,22,23] and epitaxial graphene studies[8].

It is clear that resonant peaks, present around E_D, evolve in the same fashion as E_D as a function of applied gate voltage (Fig. 2a), and persist even in low magnetic fields (Fig. 2b). We can easily identify that the resonance peaks are tied to the graphene dispersion relation, suggesting that the resonances are graphene derived states originating from impurity scattering or disorder potential, which have been a subject of recent theoretical interests in relation to the relativistic carriers of graphene[24,25]. These resonances would induce partial localization in the disorder potential, which will be reflected in magneto-transport studies.

In the presence of a perpendicular magnetic field, charge carriers in graphene circulate in cyclotron orbits with quantized energies referred to as Landau levels (LLs). As shown in Fig. 2b, the evolution of the graphene LLs can be tracked as a function of gate voltage; here at 2 T the evolution of the N=0 LL as a function of gate voltage is observed at the same location of E_D

following the identical dispersion relation as E_D at 0 T (Fig. 2a). With increasing magnetic field, additional LLs develop along with the N=0 LL[8]. Figures 2c and 2d show a series of dI/dV spectra in magnetic fields up to 8 T at V_g = -10 V (hole carriers) and V_g = 50 V (electron carriers), respectively. As expected, the N=0 LL peak develops at the location of E_D and additional LLs are distinctly resolved up to N=7 with both electron and hole carriers. It is instructive to point out that the LL linewidths are significantly broadened compared to previous reports on graphene on SiC[8,9], reflecting the shorter lifetimes and lower carrier mobility due to the substrate induced disorder potential. The LL energies follow the single-layer graphene scaling with energies that scale as $\sqrt{NB}$ and yield a carrier velocity of $(1.1 \pm 0.3) \times 10^6$ ms^{-1} (see supplement material)[26]. This value is consistent with those obtained from the analysis of E_D-dependence on V_g shown in Fig. 2

We now turn our attention to the regime where the N=0 LL is in the vicinity of E_F in the quantum Hall regime. This low density regime corresponds to the breakup of the 2D electron system into electron and hole puddles due to the variations in the disorder potential[4,6,19,20]. Figures 3, a-c show gate maps of dI/dV spectra at 8 T at different spatial locations indicated by (a), (b), and (c) in Fig. 1b, respectively. The pinning of the LLs at E_F produces a stair-case pattern of LLs in the gate maps[27-29]. Each LL is fixed at E_F until all of its degenerate states are completely filled. Then, the next available LL is pulled to E_F, with other LLs followed correspondingly. Besides, a narrow dark band observed in the vicinity of E_F is characteristic of a decrease in tunneling probability due to the development of a Coulomb gap in the quantum Hall regime[27].

An additional set of prominent features is visible in the gate maps appearing as bands of a quartet of peaks in the dI/dV spectra running diagonally. Note that the individual peaks only

cross E_F at which the particular LLs (LL_0, $LL_{\pm 1}$) are pinned. In addition, when the quartet of

peaks intersect LLs at E_F, the respective LLs and the quartet of peaks form a well defined series

of diamond structures (Figs. 3d and 3e), which are the main characteristic of Coulomb blockade

physics. We identify the four-fold peaks as single-electron charging phenomena arising from

Coulomb blockade effects in a graphene quantum dot (QD). A quartet of charging peaks has

been observed with similar STS measurements in single-walled carbon nanotube QDs[30] and can

be attributed to two valley-degenerate quantum states accommodating two electrons each (spin-

up and spin-down).

Here we assert that graphene QDs in our device are defined by the underlying disorder

potential and the incompressible (resistive) strips formed around potential hills and valleys in the

quantum Hall regime (Fig. 4a). While the Coulomb charging of localized states is known to

dominate the microscopic behavior at the Fermi energy[6,7,16], the appearance of the charging

peaks overlapping with other LLs over the large energy range of the STS measurements (Figs. 3,

a-c) is somewhat unexpected. At higher sample bias, there exist several conducting channels

contributing to individual dI/dV spectra. As illustrated in the Fig. 4b, opening of a new

conducting channel between the tip and sample Fermi levels appears as a peak in dI/dV

spectrum. Specifically, the charging resonant peaks are only seen in tunneling spectra when the

energy levels of QD are aligned to the sample Fermi level[15,30].

We note that the group of four dI/dV peaks seen at high magnetic fields emerges from a

broad band present at lower magnetic fields ($B < 4$ T) (Figs. 3f and 3g) that even exists at 0 T

(Fig. 2a). A set of dI/dV bands, as indicated with white arrows in Figs. 2a and 2b, is visible

around $V_g = 20$ V where E_D is close to E_F. The relation between this zero/low field band and the

charging peaks at high fields is apparent; both bands correspond to resonance phenomena at the

Fermi level. The bands at zero/low fields are likely caused by the scattering resonances discussed above while the quartet of charging peaks at high fields are from the resonance tunneling through quantized energy levels inside graphene QDs.

Detailed plots of dI/dV spectra displaying the evolution of a quartet of charging peaks as the magnetic field increases are shown in Figs. 3f and 3g for LL_0 near E_F (Fig. 3f), and for LL_1 at high sample bias (Fig. 3g), respectively. As dictated by Coulomb blockade physics[15], the sample bias spacing between individual dI/dV peaks is the energy required to add an additional charge into the QD. We assume that the energy spacing is mainly determined by the charging energy (E_C) because the Zeeman energy ($E_Z \approx 0.92$ meV at $B = 8$ T) is much smaller than the observed energy spacing. The charging peaks start developing around 5 T and the peak spacing is observed to be independent of magnetic field; the variance in E_C from 5 T to 8 T is around 1 meV (see supplement material).

We note that the spacing between charging peaks is uniform at the intersection with LL_1 but splits into two groups for LL_0. It is more obvious from the size variation of Coulomb diamonds revealing that the central diamond of the LL_0 is larger than other diamonds (Fig. 3d). In contrast, the size of Coulomb diamonds for the LL_1 shown in Fig. 3e is uniform. We suggest that the increased energy splitting between the second and third charging peaks is caused by the lifting of the valley degeneracy for the N=0 LL. The additional energy gap due to this symmetry breaking is estimated to be 10 meV at E_F at 8 T. Thus, we can extract E_C associated with LL_0 as (16.4 ± 0.6) meV[26], from the energy spacing for the first two and the last two charging peaks (see supplement material) in the vicinity of E_F. We can also calculate the size of the QD with E_C and capacitances obtained from the gate maps (See Methods). Given $E_C = (16.4 \pm 0.6)$ meV and the

gate map (Fig. 3b) taken at the spatial location of (b) in Fig. 1b, we can estimate the diameter of QD to be (45 ± 1) nm[26].

Detailed information on the LL spatial profile in the disorder potential and subsequent QD formation can be obtained by spatially mapping the local density of states (dI/dV signal) in the quantum Hall regime. A three-dimensional dI/dV dataset was taken with a sample bias varying from -300 mV to 300 mV and 0.4 nm spatial resolution at $B = 8$ T and $V_g = 20$ V. Similar to the characteristics of the gate map measurements, two distinct sets of features associated with either the density of states in LLs or the charging phenomena can be seen in the spatial maps. In Fig. 4c, the dominant pattern is defined by the spatial extent of the LL_0 at E_F revealing the spatial location of the graphene QD in the location (b) of Fig. 1b; a compressible (conductive) LL_0 dot is encircled by an incompressible (resistive) region that defines the QD (Fig. 4a). The map in Fig. 4d, measured at high sample bias ($V_b = 300$ mV), shows four well-resolved concentric ring-like features representing the individual Coulomb charging peaks in the QD. As the tip moves to the center of the QD, the capacitance between the tip and the QD increases, sequentially inducing electron additions to the QD. It is clear from the maps that the spatial distribution of QDs formed in Fig. 4 is highly correlated with that of electron-rich puddles and incompressible strips with hole-rich ones (Fig. 1b). This correlation explains why the charging peak separation energies are relatively insensitive to changes in magnetic field (Figs. 3f and 3g); the QD sizes are defined by the disorder potential landscape. Different QDs are also observed in different regions of the disorder potential (see supplement material).

Charging of the QDs by the tunneling electrons is sensitive to the spatial properties of the local disorder potential (Figs. 3, a-c). The bands of charging peaks intersect with LLs at the edge of the flat pinned plateau near E_F. Interestingly, this behavior is different for disorder potential

9

minima (Figs. 3a and 3b) and potential maxima (Fig. 3c).   As the density is increased by changing V_g, the next LL starts to be populated in the minima while the surrounding area remains at an integer filling factor forming an incompressible strip. Hence, for potential minima, the QD is well defined at the beginning of the plateau. An opposite evolution occurs at potential maxima; as the density is increased, the surrounding regions reach integer filling factor before the center of the potential maximum, thereby spatially defining the boundary of the QD as the LL is filled and the single-electron charging is observed at the end of the plateau. We note that the LL-transitions between pinned regions in Fig. 3 have the same slopes as the Coulomb diamonds indicating that the transitions between LLs pinned at E_F are defined by the same interactions and capacitances as the single-electron charging of the graphene QDs.

Our results demonstrate that the localization phenomena in graphene contribute to the STS spectra through two distinct set of features, one being through the density of states probed at the tunneling energy, and the other identified in the STS gate maps here, being conductance resonances at E_F. It has been well understood that the STS measurement can probe the scattering and the localization of wavefunctions leading to modulation of local density of states as a function of location and energy[5]. The sensitivity of the STS measurements to the low-energy physics at E_F was believed to quickly decay when the tunneling energy exceeds the energies of interaction and localization. However, in the general case of systems with low density of states, tip potential effectively gates the sample and modifies the transmission at the Fermi level. As a result, Fermi-level physics such as interaction and localization can be probed at much higher energies, as demonstrated here. The identification of this new channel is afforded by the unique exposure of the graphene electronic system at the surface and the tunability of localization by the application of a magnetic field.

Methods

Extracting Fermi velocity from gate maps. The Dirac point in zero magnetic field varies in energy as a function of gate voltage as $E_D = \hbar c^* \sqrt{\pi n}$, where c^* is the dispersion velocity of graphene, $n = \alpha |V_g - V_O|$ is the two-dimensional (2D) charge-carrier density induced by the applied gate potential V_g, V_O is the shift of the Dirac point created by local intrinsic doping, and α is determined by the gate capacitance. With an insulating SiO_2 layer of 300 nm thickness, α is estimated from a simple capacitor model[22,23] to be 7.19×10^{10} $cm^{-2}V^{-1}$. The dotted yellow line in Fig. 2a is the best fit of the E_D evolution with $c^* = (1.12 \pm 0.01) \times 10^6$ ms^{-1} and $V_O = (20.0 \pm 0.1)$ V[26].

Calculating the size of graphene QD from gate maps. It is straightforward to estimate the QD capacitance and the size from the Coulomb diamond features[15]. The single-electron transport through the graphene QDs is controlled by the voltages applied at the tip, contact to graphene, and the back gate through the capacitances of the vacuum gap (C_d), the incompressible strip (C_s), and the gate insulator (C_g), respectively (Fig. 4a). The ratio of capacitances obtained from the slopes of Coulomb diamonds in Fig. 3b around LL_0-pinned region, $V_g \approx 15$ V, is $C_d : C_s : C_g = 31 : 23 : 1$. The charging energy is determined by total capacitance (C_{tot}) of the QD, $E_C = e^2 / C_{tot}$, where $C_{tot} = C_d + C_s + C_g$. From the measured $E_C = (16.4 \pm 0.6)$ meV, we calculate the total capacitance of the QD, $C_{tot} = 9.8 \times 10^{-18}$ F and the gate capacitance, $C_g = 1.8 \times 10^{-19}$ F, yielding the QD diameter of (45 ± 1) nm[26].

References

1. Castro Neto, A.H., Guinea, F., Peres, N.M.R., Novoselov, K.S. & Geim, A.K. The electronic properties of graphene. *Rev. Mod. Phys.* **81**, 109-162 (2009).
2. Geim, A.K. & Novoselov, K.S. The rise of graphene. *Nature Mater* **6**, 183-191 (2007).
3. de Heer, W.A. et al. Epitaxial graphene. *Solid State Commun.* **143**, 92-100 (2007).
4. Zhang, Y., Brar, V.W., Girit, C., Zettl, A. & Crommie, M.F. Origin of spatial charge inhomogeneity in graphene. *Nature Phys* **5**, 722-726 (2009).
5. Rutter, G.M. *et al.* Scattering and Interference in Epitaxial Graphene. *Science* **317**, 219-222 (2007).
6. Martin, J. *et al.* Observation of electron-hole puddles in graphene using a scanning single-electron transistor. *Nature Phys* **4**, 144-148 (2008).
7. Martin, J. *et al.* The nature of localization in graphene under quantum Hall conditions. *Nature Phys* **5**, 669-674 (2009).
8. Miller, D.L. *et al.* Observing the quantization of zero mass carriers in graphene. *Science* **324**, 924-927 (2009).
9. Song, Y.J. *et al.* High Resolution Tunneling Spectroscopy of a Graphene Quartet. *Nature* **467**, 185-189 (2010).
10. Li, G. & Andrei, E.Y. Observation of Landau levels of Dirac fermions in graphite. *Nature Phys* **3**, 623-627 (2007).
11. Li, G., Luican, A. & Andrei, E. Scanning Tunneling Spectroscopy of Graphene on Graphite. *Phys. Rev. Lett.* **102**, 176804 (2009).
12. Miller, D.L. *et al.* Structural analysis of multilayer graphene via atomic moiré interferometry. *Phys. Rev. B* **81**, 125427 (2010).
13. Miller, D.L. *et al.* Real-space mapping of magnetically quantized graphene states. *Nature Phys* **6**, 811-817 (2010).
14. Zhang, Y. *et al.* Giant phonon-induced conductance in scanning tunnelling spectroscopy of gate-tunable graphene. *Nature Phys* **4**, 627-630 (2008).
15. Kouwenhoven, L. *et al.* Electron transport in quantum dots. *MESOSCOPIC ELECTRON TRANSPORT* **345**, 105-214 (1997).
16. Ilani, S. *et al.* The microscopic nature of localization in the quantum Hall effect. *Nature* **427**, 328-332 (2004).
17. Ishigami, M., Chen, J.H., Cullen, W.G., Fuhrer, M.S. & Williams, E.D. Atomic Structure of Graphene on SiO2. *Nano Lett.* **7**, 1643-1648 (2007).
18. Stolyarova, E. *et al.* High-resolution scanning tunneling microscopy imaging of mesoscopic graphene sheets on an insulating surface. *Proc. Natl. Acad. Sci.* **104**, 9209-9212 (2007).
19. Deshpande, A., Bao, W., Miao, F., Lau, C.N. & LeRoy, B.J. Spatially resolved spectroscopy of monolayer graphene on SiO2. *Phys. Rev. B* **79**, 205411 (2009).
20. Sarma, S.D., Adam, S., Hwang, E.H. & Rossi, E. Electronic transport in two dimensional graphene. *1003.4731* (2010). Preprint at <http://arxiv.org/abs/1003.4731>
21. Efros, A. & Shklovskii, B. Coulomb gap and low temperature conductivity of disordered systems. *J. Phys. C: Sol. Stat. Phys.* **8**, L49-L51 (1975).
22. Novoselov, K.S. *et al.* Two-dimensional gas of massless Dirac fermions in graphene. *Nature* **438**, 197-200 (2005).
23. Zhang, Y., Tan, Y., Stormer, H.L. & Kim, P. Experimental observation of the quantum Hall effect and Berry's phase in graphene. *Nature* **438**, 201-204 (2005).

24. Shytov, A.V., Katsnelson, M.I. & Levitov, L.S. Atomic Collapse and Quasi–Rydberg States in Graphene. *Phys. Rev. Lett.* **99**, 246802 (2007).
25. Shytov, A.V., Katsnelson, M.I. & Levitov, L.S. Vacuum Polarization and Screening of Supercritical Impurities in Graphene. *Phys. Rev. Lett.* **99**, 236801 (2007).
26. All uncertainties reported represent one standard deviation in the measured quantity. All uncertainties reported represent one standard deviation in the measured quantity.
27. Dial, O.E., Ashoori, R.C., Pfeiffer, L.N. & West, K.W. High-resolution spectroscopy of two-dimensional electron systems. *Nature* **448**, 176-179 (2007).
28. Dial, O.E., Ashoori, R.C., Pfeiffer, L.N. & West, K.W. Anomalous structure in the single particle spectrum of the fractional quantum Hall effect. *Nature* **464**, 566-570 (2010).
29. Efros, A. Non-linear screening and the background density of 2DEG states in magnetic field. *Solid State Commun.* **67**, 1019-1022 (1988).
30. LeRoy, B.J., Kong, J., Pahilwani, V.K., Dekker, C. & Lemay, S.G. Three-terminal scanning tunneling spectroscopy of suspended carbon nanotubes. *Phys. Rev. B* **72**, 075413 (2005).

Figure Captions

Figure 1: STM topography and STS *dI/dV* measurements at zero magnetic field. a, STM topography image, 60 nm × 60 nm, of exfoliated single-layer grahene on SiO_2/Si substrate. (inset) 3.5 nm × 3.5 nm atomic resolution image showing the graphene honeycomb lattice. Tunneling parameters: set-point current $I = 100$ pA and sample bias $V_b = -300$ mV for both images. **b,** Fixed-bias closed-loop *dI/dV* map ($V_b = -300$ mV, $V_g = 40$ V) over the same area as Fig. 1**a** revealing the spatial distribution of the disorder potential. **c,** Schematic diagram of the disorder potential variation as a function of spatial location. The relative position of the Fermi energy to the Dirac point can be tuned by an electrostatic potential from a back gate. **d,** *dI/dV* spectra taken at the top-most position of the white arrow in Fig. 1**b** showing a *dI/dV* minimum at the Dirac point. A second minimum occurs at the Fermi level (zero sample bias) along with a series of sharp resonance peaks indicated by the vertical tick marks. STS parameters: set-point

current I = 300 pA, sample bias V_b = -300 mV, root-mean-square (RMS) modulation voltage 4 mV and gate voltage V_g = 40 V. **e,** A sequence of *dI/dV* spectra taken along the white line in Fig. 1**b** showing a number of resonances that vary with the disorder potential variation. The vertical axis is the distance along the line and the horizontal axis is the sample bias. The green solid line indicates the spatial Dirac point variation ($\Delta E_D \approx$ 20 mV) along the white arrow in Fig. 1**b**. The *dI/dV* intensity is displayed in a color scale. STS parameters are the same as Fig. 1**d**.

Figure 2: **Gate and magnetic-field dependence of STS *dI/dV* spectra. a-b,** *dI/dV* gate maps taken at a fixed location (marked (b) in Fig. 1**b**) as a function of sample bias and gate voltage at 0 T and 2 T, respectively. The yellow dash-dotted lines show the evolution of the Dirac point at 0 T (LL$_0$ peak at 2 T) as a function of gate voltage. The scattering resonances observed in Figs. 1**d** and 1**e** are seen to follow the variation of the Dirac point. Broad *dI/dV* bands marked with white arrows in Figs. 2**a** and 2**b** are from the confinement by *p-n* junctions at lower magnetic fields and are evolving into a quartet of charging peaks at higher fields as seen in Fig. 3. **c-d,** Landau level spectra for various magnetic fields from 0 T to 8 T with hole (V_g = -10 V) and electron (V_g = 50 V) carriers, respectively. The *dI/dV* curves are offset for clarity. The various LL indices are indicated. The first three LLs (LL$_1$, LL$_{\pm2}$, LL$_{\pm3}$) are indicated by colored triangles in (Figs. 2 **b-d**). STS parameters: set-point current I = 300 pA, sample bias V_b = -300 mV and RMS modulation voltage 4 mV.

Figure 3: *dI/dV* gate maps around the Dirac point in the quantum Hall regime. a-c, High resolution *dI/dV* gate maps obtained at 8 T at the locations (a-c), respectively, indicated in Fig. 1**b**. Locations (a) and (b) correspond to disorder potential minima, and (c) to a maximum. **d-e,** Magnified images of the green-boxed regions in Fig. 3**a** showing Coulomb diamond features where charging lines intersect with LL$_0$ (**d**), and LL$_1$ (**e**), at the Fermi level. **f-g,** Four-fold Coulomb oscillation spectra measured for various magnetic fields from 0 T to 8 T at a fixed location (marked (b) in Fig. 1**b**) around the Fermi level for LL$_0$ (**f**) and around -220 mV for LL$_1$ (**g**) (see dotted yellow arrows in Fig. 3**b**), respectively. Note that LL$_0$ peak evolves at the Fermi level at lower magnetic fields (2 T to 4 T, in (**f**)) and Coulomb blockade effects overshadow the LL$_0$-peak development at higher fields (5 T to 8 T, in (**f**)). The unequal (**f**) / equal (**g**) spacing between charging peaks is clearly seen. The blue dots in Fig. 3**b** correspond to bias and gate voltages for the *dI/dV* maps in Figs. 4**b** and 4**c**. STS parameters: set-point current I = 300 pA, sample bias V_b = -300 mV and RMS modulation voltage 2 mV.

Figure 4: Formation of graphene QDs in the quantum Hall regime. a, Schematic of the breakup of the graphene 2DEG into interacting QDs (compressible regions) separated by insulating strips (incompressible regions) in the quantum Hall regime. Capacitances around the graphene QDs are defined in the main text. **b,** Schematic of single electron tunneling events through the graphene QD defined by two tunneling barriers (vacuum barrier and incompressible strip (I.S.) barrier) at high sample bias. Inside the QD, the Landau level pinned at the Fermi level is quantized into discrete charging levels. The incompressible strip barrier is not larger than the gap between LLs and peaks in *dI/dV* are observed when a new channel appears either at the STM tip Fermi energy (i.e. Landau level density of states) or at the Fermi level of sample (i.e. quantized states of graphene quantum dots). **c-d,** Spatial *dI/dV* maps, 60 nm × 60 nm, at V_g = 20 V and B = 8 T over the same area as in Fig. 1**a**. **c,** The map at the Fermi level (V_b = 0 mV) shows a compressible LL$_0$ region surrounded by incompressible strips, which gives rise to an

isolated graphene QD. **d,** Map of charging peaks at higher sample bias, V_b = 300 mV. These maps correspond to the locations in the gate map indicated by the blue circles in Fig. 3**b**. STS parameters: set-point current I = 300 pA, sample bias V_b = -300 mV and RMS modulation voltage 4 mV.
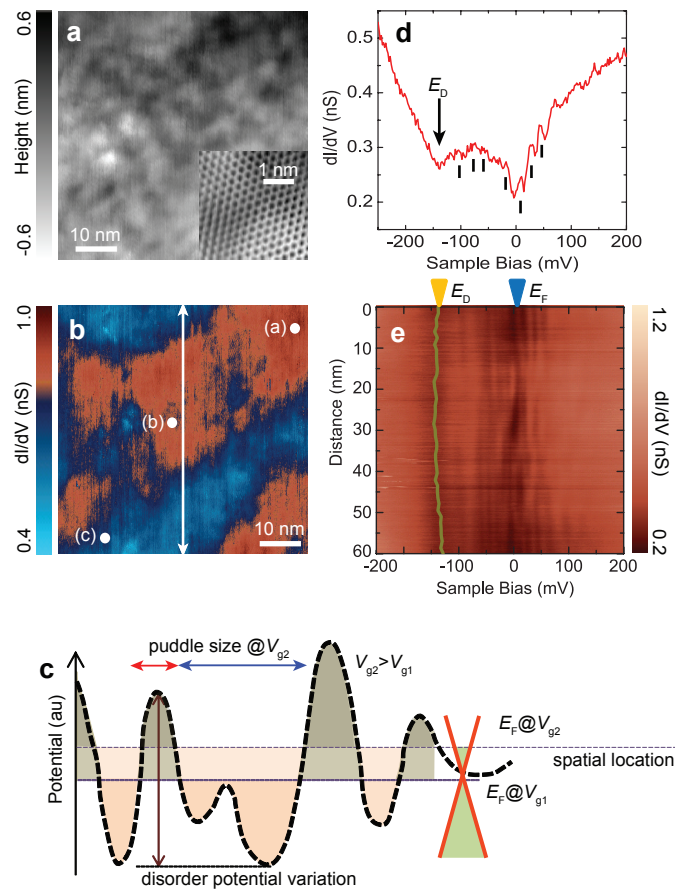
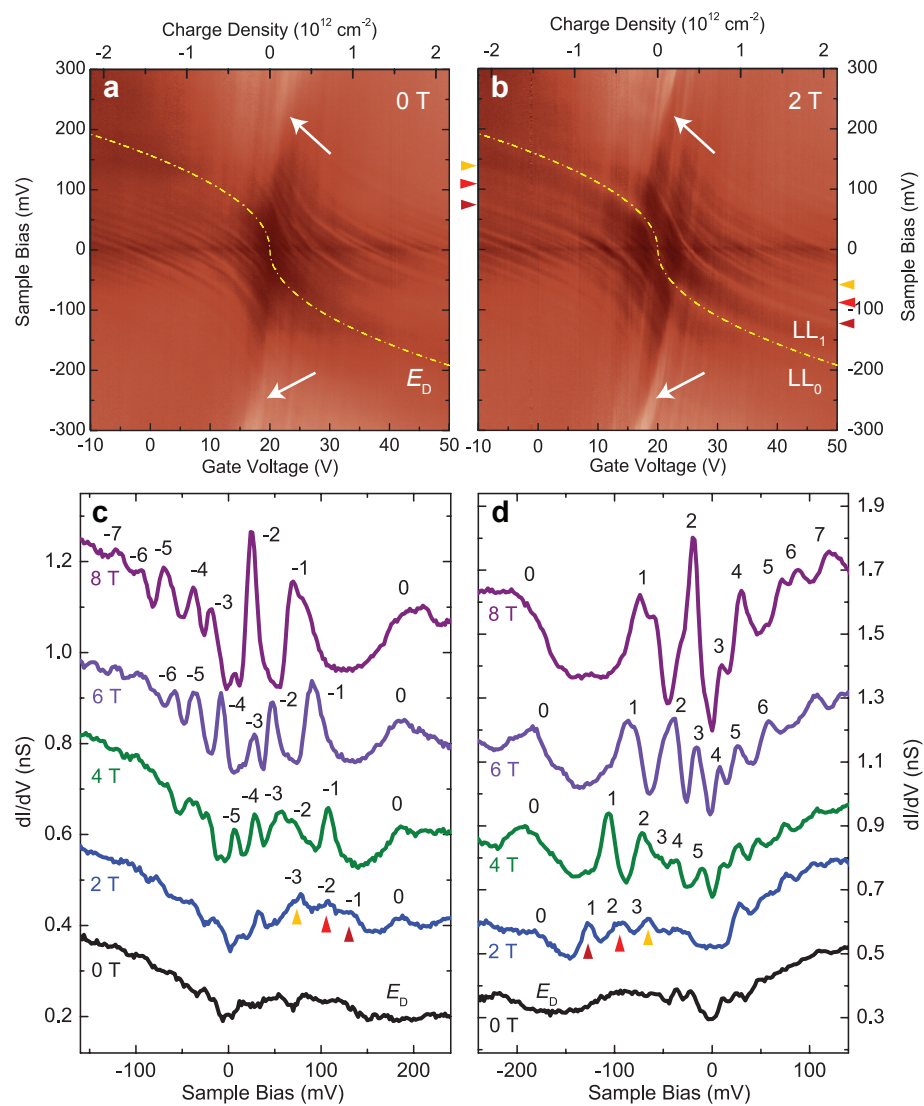**Figure 1**: **Jung et al, print full single column width 88 mm.**

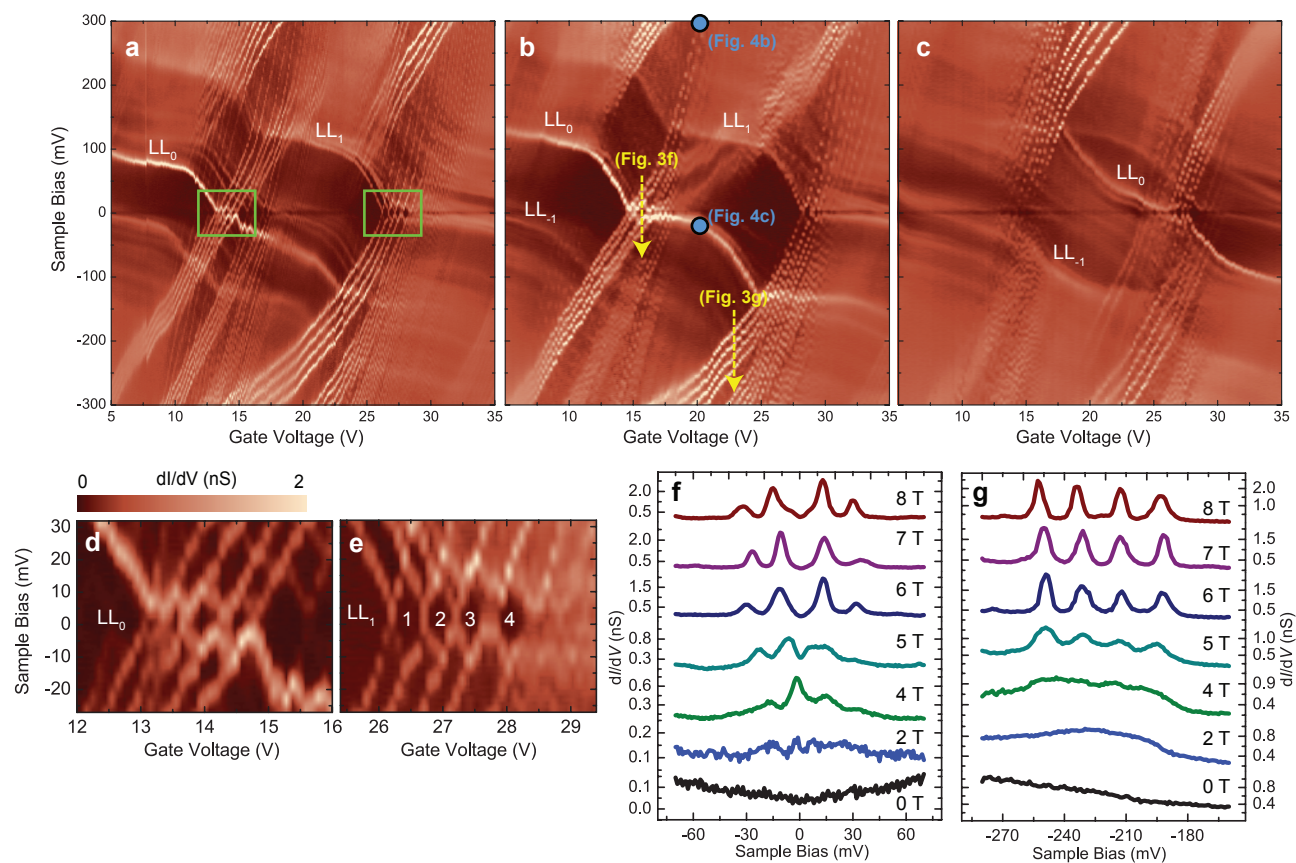**Figure 2 Jung et al, print larger than single column, 120 mm wide.**

Figure 3 Jung et al, print full double column 170 mm.

a — STM Tip, Compressible QD, C_d, Incompressible strip, QD, C_s, C_g, SiO$_2$, Si

b — Vacuum barrier, STM tip, LLs, Sample, I. S., QD, V_b, v_g

c — E=0 meV, 10 nm, Incompressible strip, Compressible QD
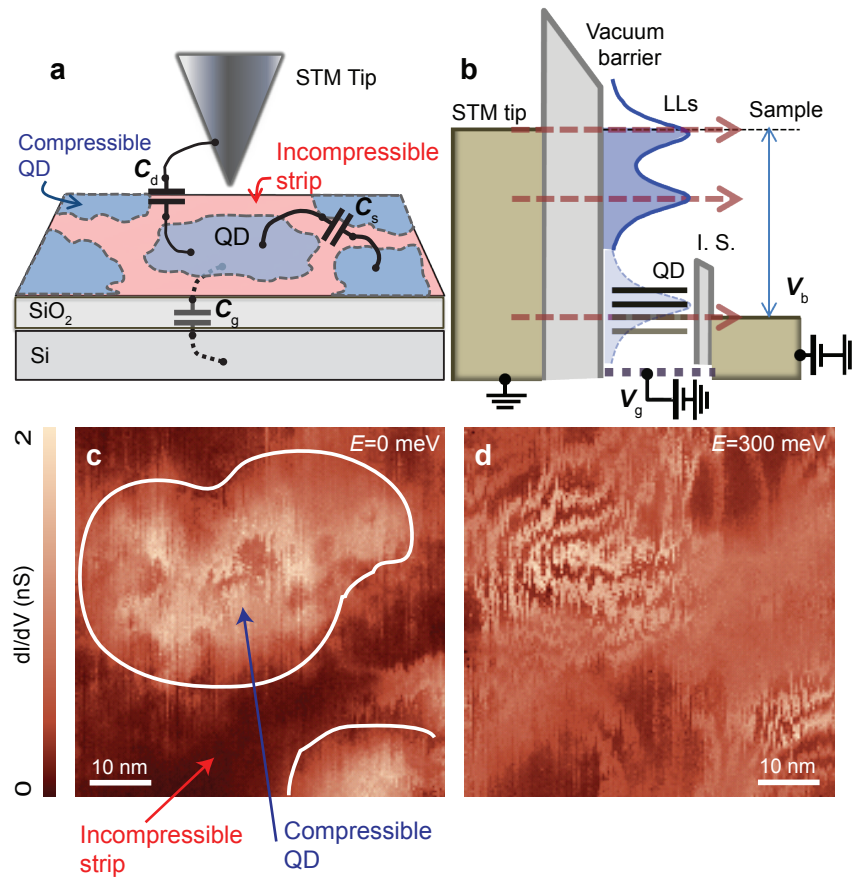
d — E=300 meV, 10 nm

dI/dV (nS)

Figure 4 Jung et al, print larger than single column, 120 mm wide.